PAPER

Temperature dependence of retarded recrystallisation in helium plasma-exposed tungsten

IOP Publishing | International Atomic Energy Agency Nuclear Fusion

Nucl. Fusion **59** (2019) 096031 (10pp) https://doi.org/10.1088/1741-4326/ab2e3c

Temperature dependence of retarded recrystallisation in helium plasma-exposed tungsten

K. Song[1], M. Thompson[1], G. De Temmerman[2] and C.S. Corr[1]

[1] Plasma Research Laboratory, Research School of Physics and Engineering, Australian National University, Canberra, Australia
[2] ITER Organization, Route de Vinon sur Verdon, CS90 046, 13067 St Paul Lez Durance Cedex, France

E-mail: kay.song@anu.edu.au

Received 9 April 2019, revised 30 May 2019
Accepted for publication 1 July 2019
Published 30 July 2019

Abstract

Recrystallisation has been identified as a critical issue for the ITER divertor but currently the synergistic effects of heat and particle bombardment on tungsten recrystallisation are still unclear. In this study, tungsten was exposed to helium plasma under a range of sample temperatures (573 K–1073 K) and ion fluences (10^{24}–10^{25} m^{-2}) followed by annealing at a range of temperatures (1373 K–1673 K). It is quantitatively found that larger helium nano-bubbles form at higher sample temperatures during plasma exposure due to increased nano-bubble mobility and coalescence. The retardation of recrystallisation showed the opposite trend, with less recrystallisation occurring in samples exposed at lower temperatures and with smaller nano-bubbles. This result is attributed to the Zener drag force from the helium nano-bubbles opposing grain boundary movements during annealing with the effect of the force being inversely proportional to bubble size. Ion fluence is not found to affect the extent of recrystallisation at any temperature. The presence of the sub-surface helium nano-bubbles increased the microstrain in the tungsten which was eliminated during subsequent annealing as a clear sign of the recovery stage proceeding.

Keywords: recrystallisation, helium plasma, tungsten, helium nano-bubbles

(Some figures may appear in colour only in the online journal)

1. Introduction

Tungsten will be used as the the plasma-facing material in the ITER divertor, withstanding heat fluxes of ~10 MW m^{-2} and a surface temperature up to 1573 K during steady state operation [1]. Slow transient events, such as during divertor reattachment, could double the heat flux on the tungsten surface over timescales of seconds and increase the surface temperature above the recrystallisation temperature of tungsten [2].

Recrystallisation is a phenomenon which occurs in polycrystalline materials annealed at high temperatures, where the initial deformed microstructure of the material is replaced by new defect-free, and typically larger, grains. This presents problems for the ITER operation as recrystallisation leads to a modification of material properties including a reduction in hardness, strength and thermal shock resistance [3]. Recrystallisation in tungsten has also been observed to lead to the pre-mature formation of macro-cracks on the surface [4, 5], accelerating material damage by grain ejection or melting. However, a more detailed understanding of the recrystallisation kinetics of tungsten exposed to conditions expected in the reactor divertor is essential to predict the material lifetime and potential impact on the ITER operation.

In the divertor, the tungsten material will be facing not only extreme heat fluxes but also high fluxes of low-energy particles, such as deuterium, tritium and helium, originating from the reactor core. It has been observed on many occasions that exposure to helium plasma can cause the production of nano-bubbles underneath the tungsten surface [6–8]. Their formation is due to the diffusion and clustering of helium atoms in

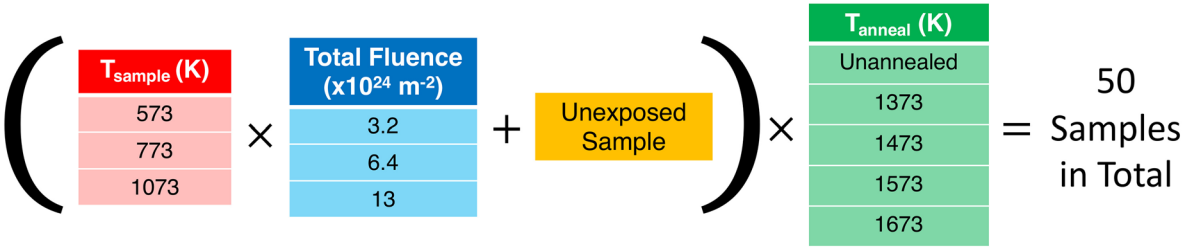

Figure 1. The total combination of all the plasma exposure and annealing conditions to produce all the samples.

the tungsten matrix [9] and the subsequent nano-bubble size increases with the temperature of the tungsten during exposure [10, 11].

It has also been found that tungsten samples heated with hydrogen plasma up to 1773 K exhibited no signs of recrystallisation while heating with neutral and electron beams caused significant recrystallisation down to millimetres below the surface [12]. A recent study has found that prior exposure to helium plasma led to a 50% reduction in percentage of recrystallised surface area when the tungsten samples were subsequently annealed for one hour at 1473 K [13]. The study also found nano-bubbles below the tungsten surface following plasma exposure.

Even though helium plasma exposure has been identified as a cause of retarded recrystallisation of tungsten, the necessary conditions for this effect to occur remain unclear. The mechanisms responsible for this effect and how the changes in helium nano-bubbles can affect tungsten recrystallisation have also not been quantified.

In this work, helium plasma exposure of tungsten at different sample temperature and total ion fluence is studied, and the effect on tungsten recrystallisation examined. The presence of helium nano-bubbles and changes to the tungsten microstructure, including grain size and microstrain, during both recovery and recrystallisation are characterised and discussed.

2. Experimental details

Tungsten samples measuring $10 \times 10 \times 2$ mm were cut from a large polycrystalline block of 99.7% purity manufactured by PLANSEE according to ITER specifications. The surface of the tungsten samples were mechanically polished to a mirror finish with silicon carbide grinding paper followed by polycrystalline diamond suspension.

Helium plasma exposures were performed in the linear plasma device MAGPIE at the ANU. Details of the device can be found in [14]. The base pressure of the device was 10^{-6} Torr. The plasma operated in pulse mode with 40%–60% duty cycle and an ion flux of 9×10^{20} m^{-2} s^{-1}. The samples were held at a floating potential during exposure which led to an ion energy of approximately 25 eV, measured from the electron temperature using a Langmuir probe. Sample temperature was controlled both by the duty cycle of the pulsed plasma and heating elements in the sample holder behind the tungsten samples. A thermocouple in contact with the back of the tungsten samples continuously monitored temperatures during exposure.

Three different sample temperatures (T_{sample}) of 573 K, 773 K and 1073 K were implemented during the plasma exposures. These temperatures were chosen to reflect a wide variety of conditions expected in the ITER divertor during operations. Previous work has also shown that at temperatures above 900 K, the nano-bubbles formed from helium plasma exposure are significantly larger [11]. This temperature range allows a practical study of different helium nano-bubble sizes and their possible effects on recrystallisation.

The samples were exposed to three different total helium ion fluences of 3.2×10^{24} m^{-2}, 6.4×10^{24} m^{-2} and 1.3×10^{25} m^{-2}. Helium reflection from tungsten has been found to depend on ion energy at below 100 eV and vary between plasma devices [15]. This may affect the ion fluence threshold for saturating nano-bubble formation from helium plasma exposure on tungsten, which is previous undetermined in the MAGPIE device. Therefore, the plasma exposure times in this experiment was chosen to cover a range of high fluences which are practically achievable in the device.

For each combination of ion fluence and sample temperature during exposure, five identical samples were exposed, each later annealed at a different temperature. Isothermal annealing for one hour was carried out at temperatures (T_{anneal}) of 1373 K, 1473 K, 1573 K and 1673 K. The annealing temperature range was chosen to study tungsten recrystallisation kinetics close to the recrystallisation temperature. The recrystallisation temperature of tungsten has been found to be approximately 1600 K [16, 17]. The previous study by Guo *et al* [13] found changes in tungsten recrystallisation behaviour following plasma exposure when annealed at temperatures between 1200 K to 1700 K, with recrystallisation occurring at approximately 1573 K.

A heating and cooling rate of 2 K min^{-1} was used for all the annealing procedures to prevent damage to the ceramic annealing tube. Annealing was carried out in a 95% N_2/5% H_2 environment with gas flow maintained at 0.8–1 l min^{-1} to prevent oxidation. Unexposed reference samples were also annealed and one of each of the exposed samples were kept unannealed for comparison. The total parameter space investigated is shown in figure 1.

Scanning electron microscopy (Zeiss UltraPlus Analytical FESEM) was used to examine changes to the surface topography after plasma exposure. Electron backscatter diffraction measurements (EBSD, Oxford Instruments HKL EBSD)

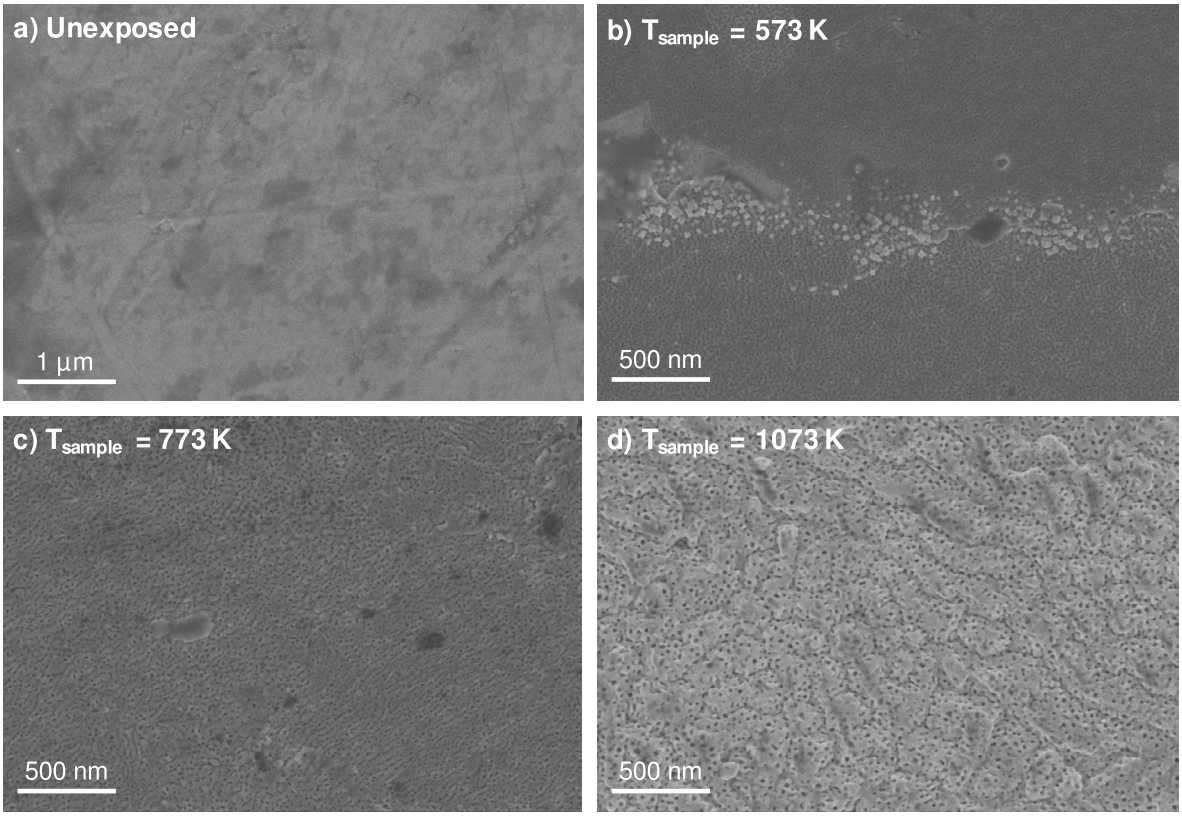

Figure 2. SEM micrographs of tungsten surfaces that are (*a*) not exposed or (*b*)–(*d*) have been exposed to an ion fluence of 1.3×10^{25} m^{-2} at different T_{sample}. All exposed samples show pinholes on the surface which increase in size with T_{sample}.

analysed with the Channel 5 Tango software package were used to determine grain size distributions.

Grazing-incidence small-angle x-ray scattering (GISAXS) was performed at the Australian Synchrotron with 10 keV x-rays and a camera length of 961 mm. These conditions were chosen to best measure sub-surface helium nano-bubble sizes between 1–10 nm. GISAXS data was analysed by fitting to the model described in [18]. The nano-bubbles were modelled as spheroids, with the axis of rotation normal to the sample surface, and with a log-normal distribution of radii. Grazing-incidence x-ray diffraction (GIXRD, Hi-resolution PANalytical X'Pert PRO MRD) was used to measure material microstrain near the surface of the tungsten through Williamson–Hall plot analysis [19]. The grazing-incidence angle of 1° ensures that the measurements are more weighted toward the top sub-surface region which contains the helium nano-bubbles.

3. Results

3.1. Surface morphology after plasma exposure

Changes to tungsten surface morphology after plasma exposure is used to deduce sub-surface information. Figure 2 shows that after plasma exposure, there are small pinholes on the surface, which increase in size with T_{sample}, and similar features have been observed in another study [20]. They are likely caused by helium nano-bubbles formed close to the surface which grow and push away surface tungsten material, leaving behind holes [21].

At $T_{sample} = 573$ K, there appears to be some tungsten nanostructural growth, verified using energy-dispersive x-ray spectroscopy, occurring on the grain boundaries and some grain-dependent roughening which change the apparent size of the surface pinholes. Increasing T_{sample} appears to enlarge the pinholes on the surface (figures 2(*c*) and (*d*)) and this can be explained by considering the increased mobility of the helium atoms and clusters with temperature, resulting in larger helium nano-bubbles.

At the highest temperature, large surface pits, greater than 20 nm in diameter, can be observed, suggesting the presence of large sub-surface nano-bubbles. Sharafat *et al* [22] have presented evidence that the helium nano-bubbles themselves become mobile at above 1073 K and contribute significantly to nano-bubble growth by merging and coalescence. This mechanism likely explains the large surface pits formed at this temperature. At $T_{sample} = 1073$ K, the surface appears to exhibit a wavy morphology, which have also been observed in a previous study [23].

3.2. Quantitative GISAXS analysis of Nano-bubbles

GISAXS measurements were able to probe the distribution of sub-surface helium nano-bubble radii. The raw scattering images obtained are shown in figure 3. The scattering pattern from the unexposed sample consist of only a central streak due to scattering from surface roughness. In contrast, the presence of sub-surface nano-bubbles cause a semi-circular to triangular scattering pattern, and this pattern is fitted according to the methods described in a previous GISAXS study [18]

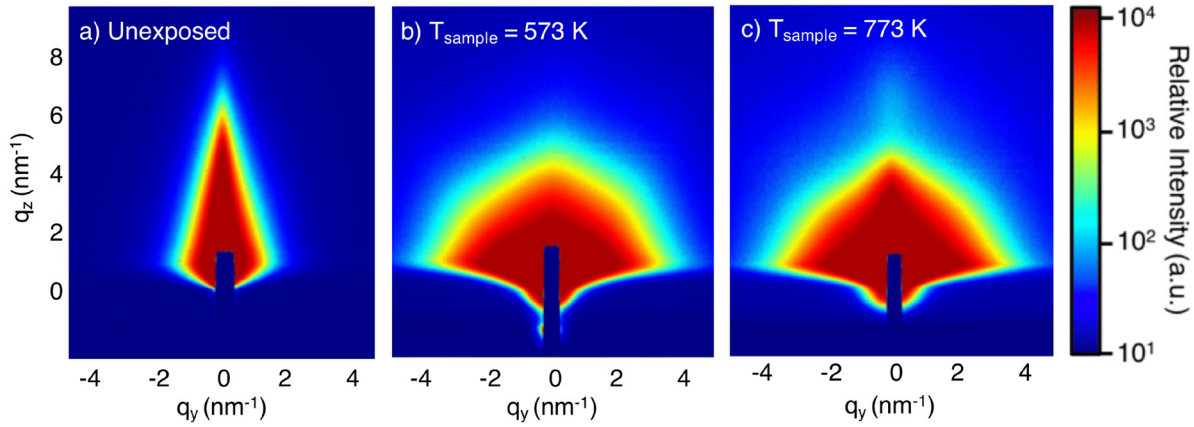

Figure 3. The scattering patterns collected from unannealed samples. The plasma-exposed samples received a helium fluence of 1.3×10^{25} m^{-2}.

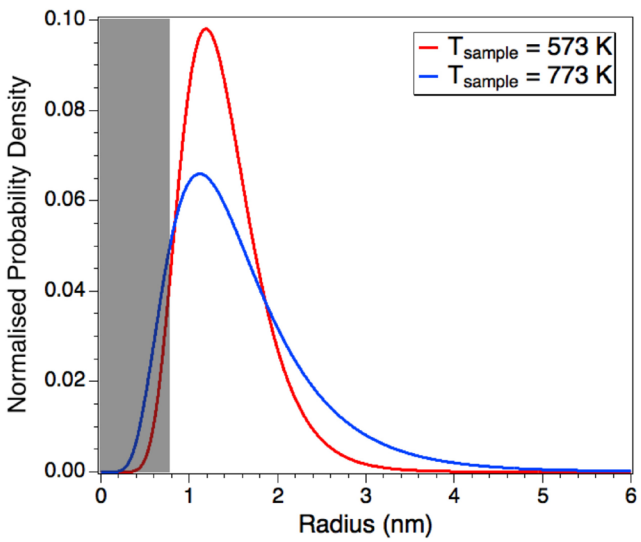

Figure 4. The distribution of bubble radii fitted to a log-normal distribution in the samples exposed at $T_{sample} = 573$ K and 773 K to an ion fluence of 1.3×10^{25} m^{-2}. Higher T_{sample} leads to a larger distribution of bigger nano-bubbles. The grey box covers the region of the radius range which cannot be directly probed during the measurements.

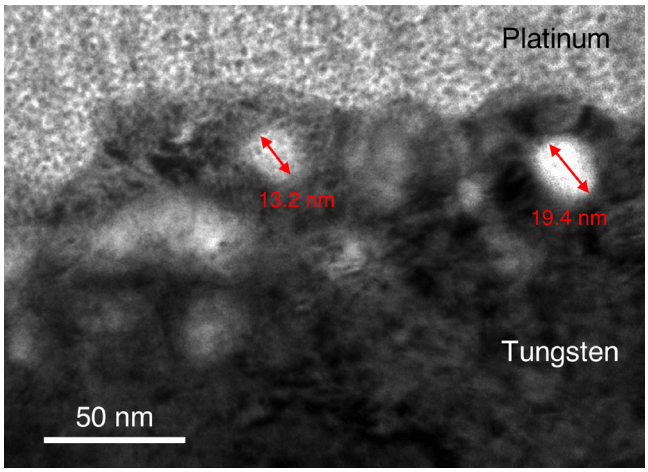

Figure 5. Cross-section transmission electron micrograph of the sub-surface helium nano-bubbles formed after exposure at $T_{sample} = 1073$ K to an ion fluence of 1.3×10^{25} m^{-2}. Nano-bubbles up to 20 nm in diameter can be observed. The TEM lamina was prepared using focused-ion beam with a protective platinum layer on the surface of the tungsten. Due to the limitations in sample preparation, bubbles smaller than 5 nm could not be imaged clearly.

in order to extract the normalised size distribution of the nano-bubbles.

Figure 4 shows the fitted distributions of the nano-bubble sizes for tungsten exposed to a helium ion fluence of 1.3×10^{25} m^{-2} at $T_{sample} = 573$ K and 773 K. The mean nano-bubble size for $T_{sample} = 573$ K is 1.4 ± 0.1 nm while for $T_{sample} = 773$ K, it is 1.6 ± 0.2 nm. The errors are calculated as the standard deviations of the mean values from ten independent fits. For the $T_{sample} = 773$ K, the plotted distribution also clearly shows a higher population of larger nano-bubbles, which is in agreement with the SEM observations of the surface pinhole sizes in figure 2. These results also agree with transmission electron microscopy observations from previous studies of nano-bubble diameters around 1–2 nm [6, 7, 24].

For the highest T_{sample} of 1073 K, the scattering pattern contains more complex features that are not compatible with the current spheroid model used for the lower temperatures. The greater extent of surface reorganisation also significantly compromises the accuracy of fitting with the current model. Figure 5 shows a transmission electron micrograph of the sub-surface bubbles at $T_{sample} = 1073$ K and nano-bubbles up to 20 nm in diameter can be observed below the tungsten surface. The limited resolution of this measurement imposes a lower bound on the size of the nano-bubbles observed and the larger nano-bubbles are likely to be over-represented. Nevertheless, it can be concluded from the surface pinholes, the GISAXS and TEM data that sub-surface helium nano-bubble sizes increase with temperature during exposure. Further TEM studies with better sample preparation to increase resolution are already under way to improve the nano-bubble size measurements and contribute to a more comprehensive model for GISAXS fitting.

3.3. Recrystallisation behaviour

The extent of recrystallisation was characterised by comparing the surface coverage of deformed and recrystallised

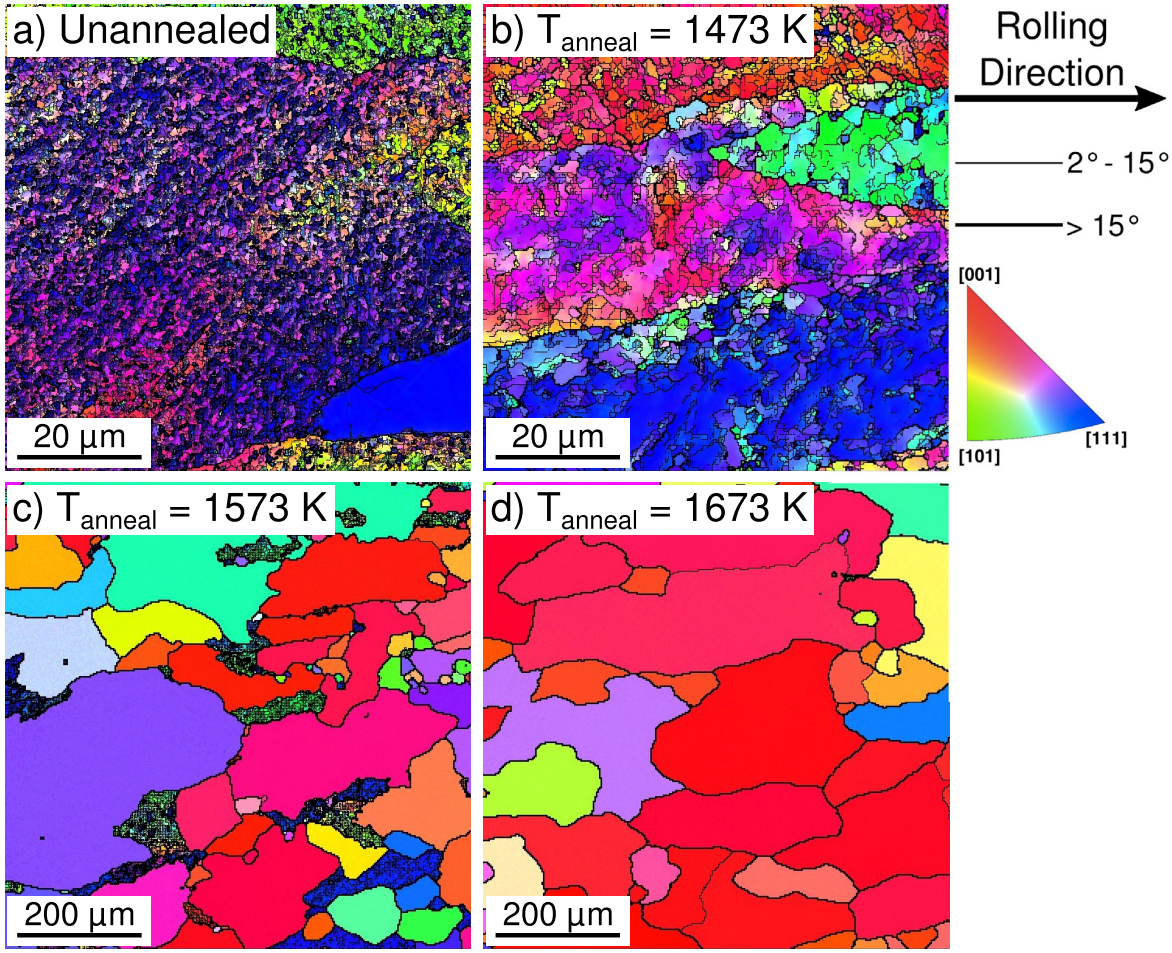

Figure 6. Surface normal direction IPF map of unexposed tungsten after various annealing temperatures. Note the factor of ten scale difference between (*a*)/(*b*) and (*c*)/(*d*). The distinct change in grain sizes and internal dislocations after annealing at 1573 K and 1673 K respectively show the onset and completion of recrystallisation.

grains, which are much larger than deformed grains and also do not have any internal dislocations or subgrains. EBSD has been used to measure surface grain changes in tungsten as a function of sample temperature during plasma exposure, ion fluence and annealing temperature.

3.3.1. Without prior plasma exposure. Figure 6 shows the inverse polar figure (IPF) maps of the tungsten surfaces before and after annealing for the samples without exposure to helium plasma. For the unannealed sample in figure 6(*a*), the sampled area is mainly covered by one large deformed grain consisting of many small subgrains separated by low angle grain boundaries (2°–15°), indicated by the thin black lines.

Figures 6(*b*)–(*d*) show increasing grain size with T_{anneal}. The different stages of material changes during annealing can be identified as recovery (figure 6(*b*)), partial recrystallisation (figure 6(*c*)) and complete recrystallisation (figure 6(*d*)). These measurements indicate that for a 1-hour annealing, the temperature threshold for recrystallisation occurs between 1473 K to 1573 K. It also appears that after annealing at 1673 K, no observable progression of the grain growth stage has occurred as the recrystallised grains appear elongated along the original rolling direction. It is expected with further annealing the grains will become more equiaxed to further lower the stored energy by reducing the curvature of the grain boundaries.

3.3.2. Recrystallisation after plasma exposure. The effect of plasma exposure on recrystallisation is most prominent for an annealing temperature of 1673 K. Figure 7 shows the comparison of the EBSD results and it is clear that all samples exposed to plasma are less recrystallised compared to the unexposed sample. Figure 7(*b*) shows that the strongest retardation of recrystallisation occurred for plasma exposure at $T_{\text{sample}} = 573$ K as there are many more deformed grains present on the surface than the other plasma-exposed samples. In figures 7(*c*) and (*d*), the surfaces of samples with $T_{\text{sample}} = 773$ K and 1073 K also show some small deformed grains but their total coverage of the sample is much smaller in comparison to $T_{\text{sample}} = 573$ K.

Figure 8(*a*) shows a quantitative comparison of the percentage of the sampled area covered by deformed grains, which are defined as areas with average internal subgrain misorientation greater than 2°. The results agree with the qualitative observations of the IPF maps in figure 7. The unexposed sample has almost no deformed grains as it is fully recrystallised. For $T_{\text{sample}} = 573$ K, over 8% of the surface was covered

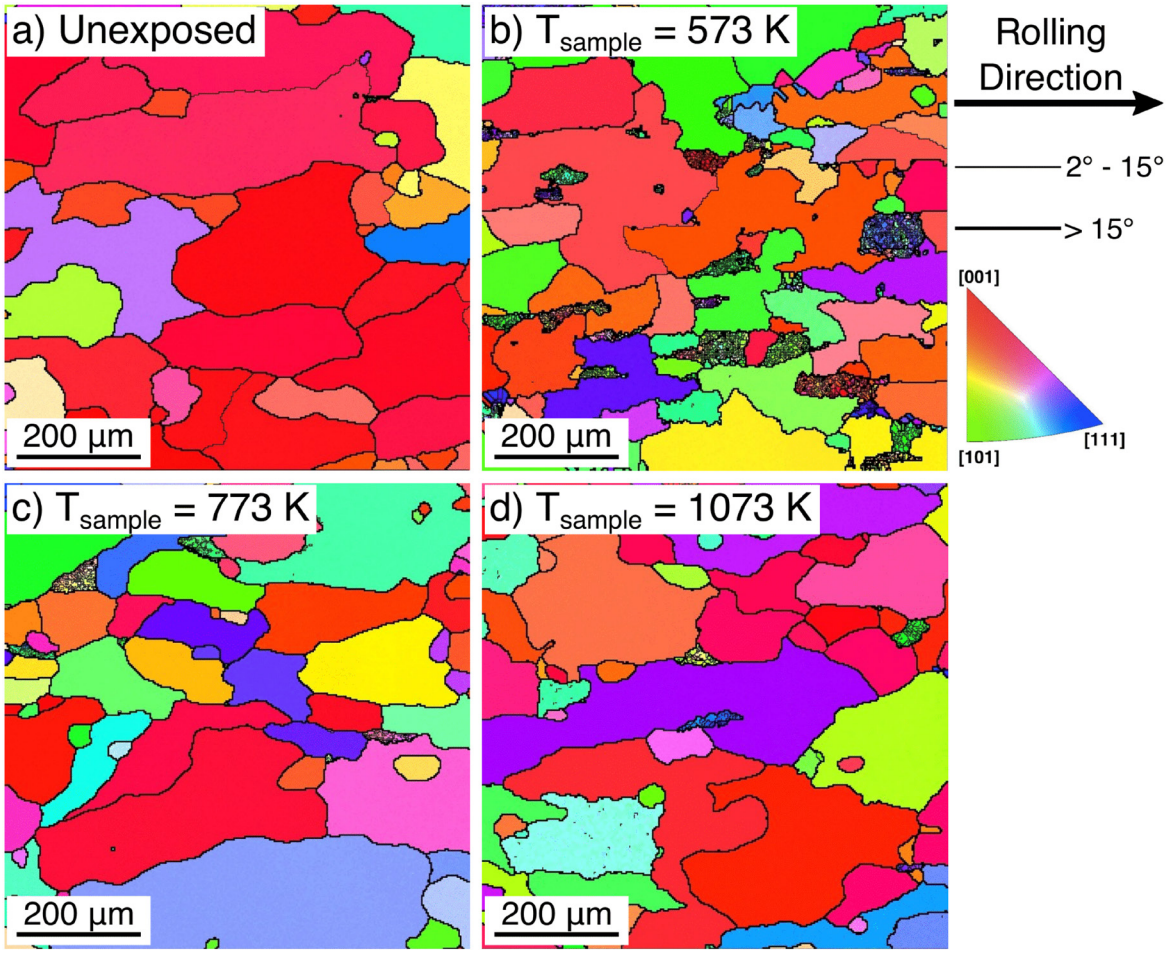

Figure 7. Surface normal direction IPF maps of (*a*) the unexposed sample, and (*b*)–(*d*) samples exposed to an ion fluence of 1.3×10^{25} m^{-2} with different T_{sample}. All samples were subsequently annealed at 1673 K for one hour. The unexposed sample has completely recrystallised. Plasma exposure with sample temperature at 573 K clearly shows the most retarded recrystallisation as it has the largest area of deformed grains.

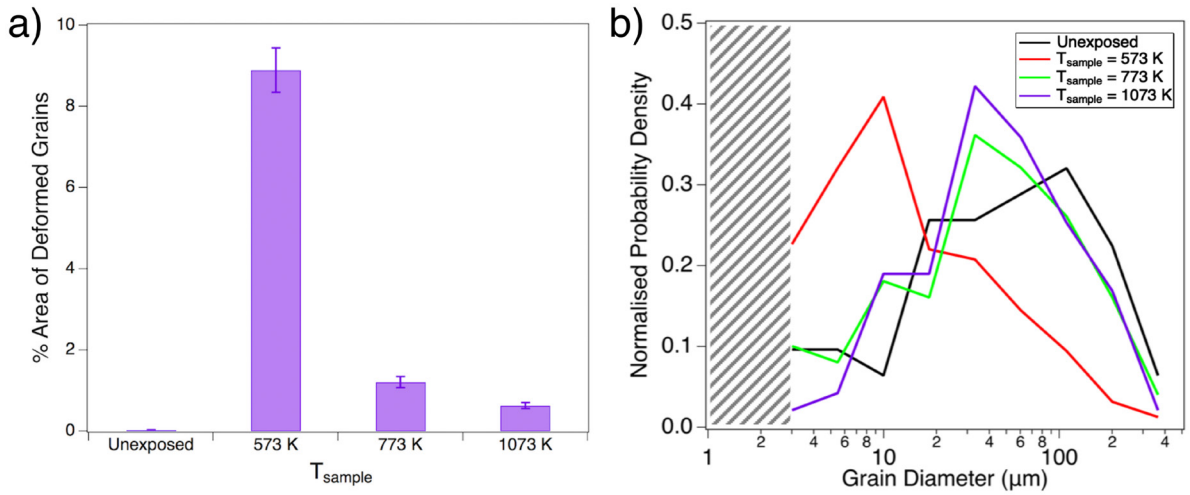

Figure 8. (*a*) The area covered by deformed grains on unexposed and plasma-exposed samples all annealed for one hour at 1673 K. The error bars are estimated based on estimating the size distribution of the grains as Poissonian. (*b*) The distribution of grain sizes in the samples, with grains defined as regions with a misorientation of at least 15° at the boundaries. The grey region indicates the range of sizes unable to be measured due to the step size of the EBSD measurements. Both figures support the results of the orientation maps in figure 7 that tungsten exposed to plasma at 573 K has the least amount of recrystallisation.

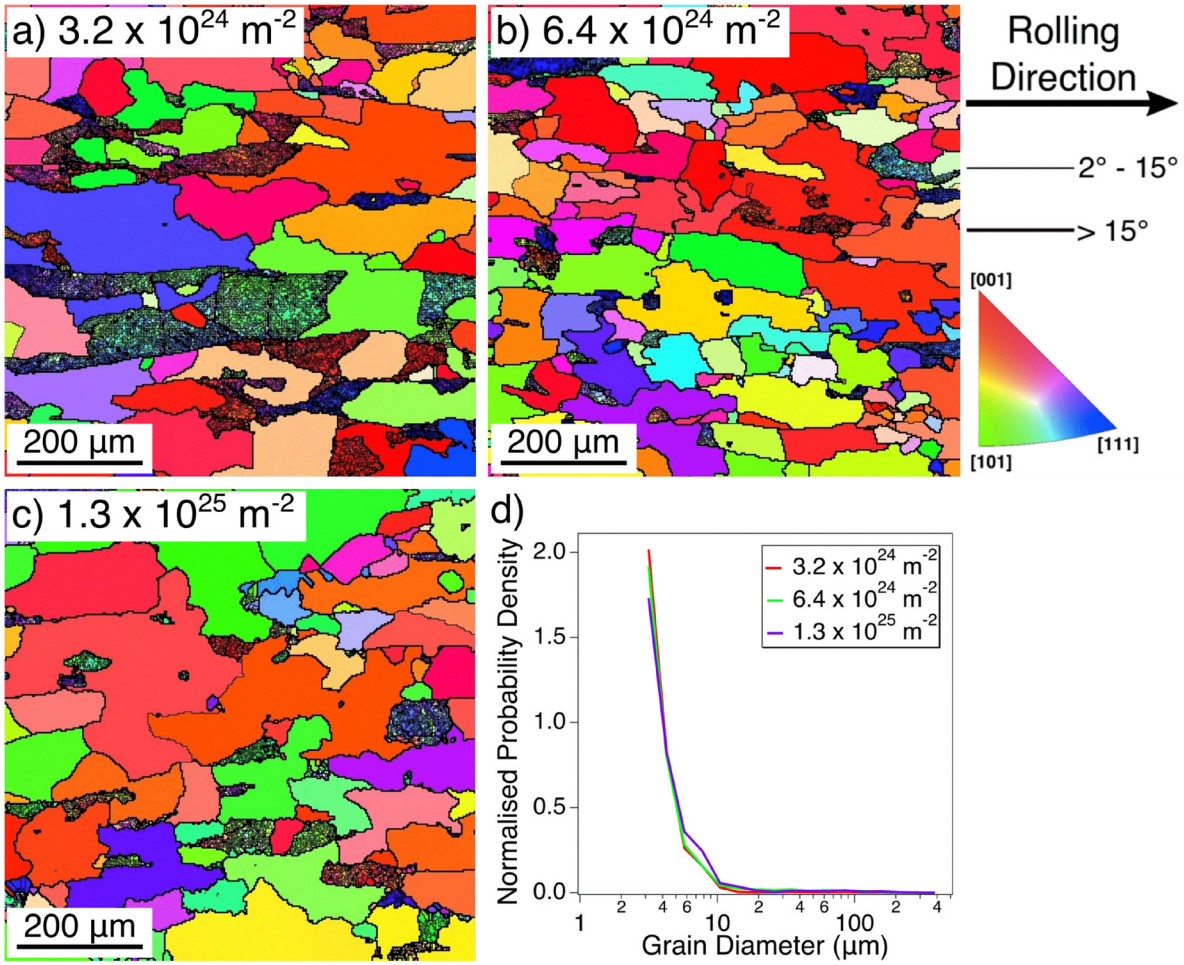

Figure 9. The IPF maps of samples exposed to different ion fluences while held at $T_{\text{sample}} = 573$ K and then subsequently annealed at $T_{\text{anneal}} = 1673$ K. There is no statistical difference in the extent of recrystallisation between the samples.

by deformed grains. This is over five times higher than those exposed with $T_{\text{sample}} = 773$ K and 1073 K.

In order to estimate the errors of the coverage percentage values, the number of small subgrains counted within deformed grains in the sampled areas, n, is approximated as following a Poisson distribution. Therefore the relative uncertainty of the number of subgrains is given by $\frac{1}{\sqrt{n}}$. A better uncertainty estimation can be made if more areas of the surface are measured. The distribution of deformed grains in maps in figure 7 appear fairly homogeneous and likely representative of each sample surface.

Figure 8(*b*) shows the normalised distribution of grain sizes in the IPF maps shown in figure 7. The plot highlights the progression of the recrystallisation extent through changes in the grain sizes for the samples exposed with different T_{sample}. There is a significant difference in the mode diameter of the grains between $T_{\text{sample}} = 573$ K and $T_{\text{sample}} = 773$ K–1073 K. This again highlights the major difference in the extent of recrystallisation as the deformed grains are typically much smaller than the recrystallised grains. The unexposed sample is the most recrystallised in comparison, as it has the greatest number of grains (area under the curve) greater than 20 μm in diameter.

To explain these results, we consider that the presence of second-phase particles, such as oxides, in materials can oppose

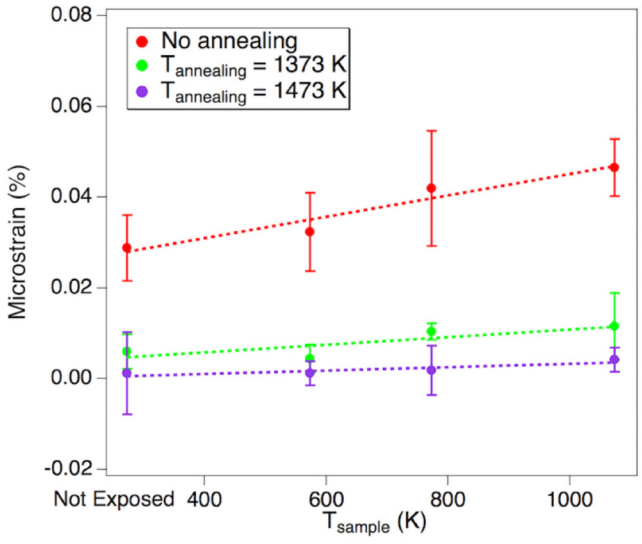

Figure 10. The measured microstrain in the samples subjected to various plasma and annealing treatments obtained by the Williamson–Hall plot method. The plasma-exposed samples all received an ion fluence of 1.3×10^{25} m^{-2}. The error bars for each data point represent one standard deviation in the linear fit of the peak widths for the Williamson–Hall plot. There is an increase of microstrain with T_{sample} particularly before annealing. After annealing at 1473 K, the microstrain values for all samples are close to zero.

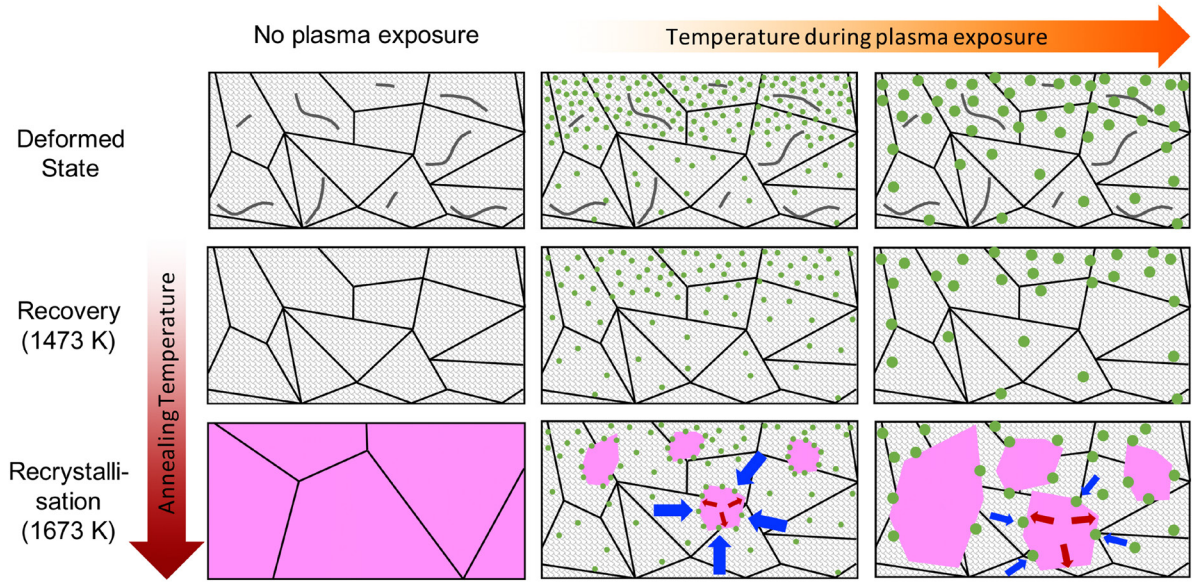

Figure 11. Summary of the changes to tungsten samples observed in this study due to changes in T_{sample} and T_{anneal}. Increasing T_{sample} causes the formation of larger sub-surface nano-bubbles. However, smaller nano-bubbles were found to exert a greater Zener drag compared to larger nano-bubbles, and more prominent retarded recrystallisation was observed after subsequent annealing at 1673 K.

the movement of grain boundaries during annealing, termed Zener drag, and delay the onset of recrystallisation [25]. Gas-filled pores in copper have been found to act as second-phase particles which retard recrystallisation [26]. Retarded recrystallisation has also been observed in potassium-doped tungsten, where the potassium exist as bubbles surrounding the tungsten grains [27]. In this case, the presence of the helium nano-bubbles could also be behaving as second-phase particles and exert Zener drag on the grain boundaries, which explains the retarded recrystallisation. The samples which underwent the least recrystallisation correspond to those that have the smallest average bubble radii observed in the SEM and GISAXS measurements. This is further evidence of the Zener drag as its mathematical form is:

$$F_{Zener} = \frac{3f_v\gamma}{2r} \quad (1)$$

where r is the radius of the helium nano-bubbles, f_v is the volume fraction of the nano-bubbles and γ is the energy of the pinned grain boundary. This description shows that smaller nano-bubbles will exert greater total Zener drag forces on the grain boundaries for a given total volume fraction of nano-bubbles. The experimental results agree with this—smaller nano-bubbles presented a greater opposing force to the boundary movements during annealing and resulted in samples with the most retarded recrystallisation.

This explanation assumes that the volume fraction of the nano-bubbles is the same in the samples. The volume fractions of the nano-bubbles have not been measured in this study but we can approximate from results of a previous study on helium retention by Ryabtsev *et al* [28]. They found that helium retention decreases slightly with irradiation temperature between 300 K to 1200 K. They also found that the temperature effect on retention decreases with ion fluence and becomes almost insignificant at an ion fluence of 10^{22} m^{-2}. Taking these previous helium retention results into consideration, it is likely in the samples of this study, the helium retention and volume fraction of the nano-bubbles are fairly similar. In combination with the dependence of helium nano-bubble size on exposure temperature, this strongly supports that the different magnitude of Zener drag resulting from the helium nano-bubbles in the tungsten matrix are responsible for the varying degrees of recrystallisation observed.

The other assumption of constant γ between the samples can be justified by considering that recrystallisation mainly involves the movement of high angle grain boundaries which have similar energies [29]. Furthermore, the small energy difference between different boundaries are insignificant and average out when many grain boundaries are considered across the whole sample.

3.3.3. Effect of ion fluence. Figure 9 shows that there is no significant microstructural difference for samples held at $T_{sample} = 573$ K exposed to different ion fluences. Though the IPF maps do not appear identical, the statistical distribution of grain sizes, shown in figure 9(*d*), are the same for all three samples, indicating the same extent of retarded recrystallisation.

In a previous TEM study by Kajita *et al*, helium nano-bubble saturation at high ion fluences above 10^{23} m^{-2} have been observed [10]. It is likely in this case that nano-bubble saturation has also occurred in the samples observed in this study. The constant density of nano-bubbles present in samples which exhibit similar extent of recrystallisation further supports that retarded recrystallisation result from the Zener drag exerted by the nano-bubbles.

3.4. Microstrain during recovery

The measurement of crystallite microstrain with GIXRD revealed changes in the material due to plasma exposure and annealing during the recovery stage. Figure 10 shows the microstrain of the samples as a function of T_{sample} and T_{anneal}.

It can be seen that without annealing, the microstrain of the samples is greater after exposure to plasma and increases with T_{sample}. The microstrain for $T_{sample} = 1073$ K is over 61% higher than the unexposed material and 44% higher than $T_{sample} = 573$ K.

The higher value of microstrain for larger T_{sample} corresponds to more deformation of the tungsten lattice due to larger helium nano-bubbles present. This results in more stored energy available within the tungsten system to drive recrystallisation. Thus it could partly explain the findings of figure 8 as the increased stored energy driving grain boundaries movement competes with the Zener drag force which reduces the retarding effect of the helium nano-bubbles during recrystallisation.

With increased annealing temperature, the microstrain decreases in all samples regardless of exposure to plasma. This is a clear sign of recovery, as the microstrain decreases when the stored energy is utilised to move dislocations and defects into more energetically-favourable locations.

The dependence of microstrain on T_{sample} disappears after annealing. Even at $T_{anneal} = 1373$ K, all samples appear to have the same microstrain within the measurement uncertainty.

After annealing at 1473 K, all samples have almost no measured microstrain, suggesting that some helium nano-bubbles have been removed from the samples and the material is largely restored. Given that the initial microstrain is larger for higher T_{sample}, this indicates the rate of recovery at 1473 K also increases with T_{sample} due to more initial stored energy. Similar results have been found previously in aluminium [30, 31].

4. Summary and conclusion

This study confirms the role of helium plasma exposure and helium nano-bubble creation on the recrystallisation kinetics of tungsten. Recrystallisation was found to be most retarded when plasma exposure resulted in smaller sub-surface nano-bubbles. Figure 11 shows a schematic representation of the tungsten samples in this study under different plasma exposure and annealing conditions.

In the deformed state, the tungsten has high levels of microstrain due to the manufacturing and mechanical polish processes. The size of helium nano-bubbles from plasma exposure in unannealed tungsten increases with T_{sample}. This is attributed to the merging and coalescence of more mobile nano-bubbles at higher temperatures and is also consistent with previous observations in literature [6, 7, 10]. The presence of the nano-bubbles is the cause of increased microstrain after plasma exposure and the microstrain increases with nano-bubble size, as a larger region of the lattice is distorted. Higher microstrain values correspond to increased stored energy in the material, driving recrystallisation.

Exposures to helium plasma did not have an impact on the final extent of recovery before the onset of recrystallisation at 1473 K. All samples show no microstrain after annealing at 1473 K. However, the difference in microstrain observed in the samples before annealing suggests that the rate of recovery is also higher for samples with initially higher strain. This can be justified by considering that stored energy increases with strain, which drives the higher rates of recovery. It is also likely that many helium nano-bubbles also escaped from the tungsten matrix to relieve the microstrain.

All plasma-exposed samples showed retarded recrystallisation compared to the unexposed tungsten after annealing at 1673 K. This is attributed to the Zener drag force exerted by the helium nano-bubbles on the grain boundaries, reducing their mobility during annealing. The smaller nano-bubbles were linked to larger Zener drag compared to bigger nano-bubbles, and caused the greatest suppression of recrystallisation.

Ion fluence was not found to change the extent of recrystallisation or recovery in this study which can be explained by the saturation of helium nano-bubble densities at ion fluences above 10^{24} m^{-2}.

The results of this study indicate a plasma-exposure temperature dependence for the extent of tungsten recrystallisation, which is crucial to account for in divertor operations. This effect has been attributed to the different sub-surface nano-bubble sizes which are temperature-dependent, with smaller nano-bubbles exerting larger Zener drag forces on grain boundary movements. Future studies with TEM to verify nano-bubble densities have been planned to confirm this.

Acknowledgments

We acknowledge assistance from ANSTO with the provision of the tungsten samples. The GISAXS measurements were taken with help from the team on the SAXS/WAXS beam line at the Australian Synchrotron, Victoria, Australia. The EBSD and SEM images were taken with the help from Dr Hua Chen at the ANU Centre for Advanced Microscopy. We are also grateful for the helpful discussions provided by Dr Long Cheng from Beihang University. This work is supported by the Australian Government through the National Collaborative Research Infrastructure Strategy Program.

The views and opinions expressed herein do not necessarily reflect those of the ITER Organization.

ORCID iDs

K. Song https://orcid.org/0000-0001-8011-3862
M. Thompson https://orcid.org/0000-0002-2354-484X
G. De Temmerman https://orcid.org/0000-0002-4173-0961
C.S. Corr https://orcid.org/0000-0002-1793-3873

References

[1] Pitts R.A. *et al* 2013 A full tungsten divertor for ITER: physics issues and design status *J. Nucl. Mater.* **438** S48–56
[2] De Temmerman G., Hirai T. and Pitts R.A. 2018 The influence of plasma-surface interaction on the performance of tungsten at the ITER divertor vertical targets *Plasma Phys. Control. Fusion* **60** 044018
[3] Raabe D. 2014 Recovery and recrystallization: phenomena, physics, models, simulation *Physical Metallurgy* (Amsterdam: Elsevier) pp 2291–397

[4] Panayotis S. *et al* 2017 Self-castellation of tungsten monoblock under high heat flux loading and impact of material properties *Nucl. Mater. Energy* **12** 200–4

[5] Panayotis S., Hirai T., Barabash V., Amzallag C., Escourbiac F., Durocher A., Komarov V., Martinez J. and Merola M. 2017 Fracture modes of ITER tungsten divertor monoblock under stationary thermal loads *Fusion Eng. Des.* **125** 256–62

[6] Iwakiri H., Yasunaga K., Morishita K. and Yoshida N. 2000 Microstructure evolution in tungsten during low-energy helium ion irradiation *J. Nucl. Mater.* **283–7** 1134–8

[7] Yoshida N., Iwakiri H., Tokunaga K. and Baba T. 2005 Impact of low energy helium irradiation on plasma facing metals *J. Nucl. Mater.* **337–9** 946–50

[8] Nishijima D., Ye M., Ohno N. and Takamura S. 2004 Formation mechanism of bubbles and holes on tungsten surface with low-energy and high-flux helium plasma irradiation in NAGDIS-II *J. Nucl. Mater.* **329–33** 1029–33

[9] Perez D., Vogel T. and Uberuaga B.P. 2014 Diffusion and transformation kinetics of small helium clusters in bulk tungsten *Phys. Rev.* B **90** 14102

[10] Miyamoto M., Mikami S., Nagashima H., Iijima N., Nishijima D., Doerner R., Yoshida N., Watanabe H., Ueda Y. and Sagara A. 2015 Systematic investigation of the formation behavior of helium bubbles in tungsten *J. Nucl. Mater.* **463** 333–6

[11] Thompson M., Doerner R., Ohno N., Kirby N., Kluth P., Riley D. and Corr C. 2017 Measuring temperature effects on nano-bubble growth in tungsten with grazing incidence small angle x-ray scattering *Nucl. Mater. Energy* **12** 1294–7

[12] Loewenhoff T., Bardin S., Greuner H., Linke J., Maier H., Morgan T.W., Pintsuk G., Pitts R.A., Riccardi B. and De Temmerman G. 2015 Impact of combined transient plasma/heat loads on tungsten performance below and above recrystallization temperature *Nucl. Fusion* **55** 123004

[13] Guo W., Cheng L., De Temmerman G., Yuan Y. and Lu G.-H. 2018 Retarded recrystallization of helium-exposed tungsten *Nucl. Fusion* **58** 106011

[14] Blackwell B.D., Caneses J.F., Samuell C.M., Wach J., Howard J. and Corr C. 2012 Design and characterization of the magnetized plasma interaction experiment (MAGPIE): a new source for plasma—material interaction studies *Plasma Sources Sci. Technol.* **21** 055033

[15] Borovikov V., Voter A.F. and Tang X.-Z. 2014 Reflection and implantation of low energy helium with tungsten surfaces *J. Nucl. Mater.* **447** 254–70

[16] Mathaudhu S.N., DeRosset A.J., Hartwig K.T. and Kecskes L.J. 2009 Microstructures and recrystallization behavior of severely hot-deformed tungsten *Mater. Sci. Eng.* A **503** 28–31

[17] Alfonso A., Juul Jensen D., Luo G.-N. and Pantleon W. 2014 Recrystallization kinetics of warm-rolled tungsten in the temperature range 1150–350 C *J. Nucl. Mater.* **455** 591–4

[18] Thompson M., Sakamoto R., Bernard E., Kirby N., Kluth P., Riley D. and Corr C. 2016 GISAXS modelling of helium-induced nano-bubble formation in tungsten and comparison with TEM *J. Nucl. Mater.* **473** 6–12

[19] Williamson G.K. and Hall W.H. 1953 X-ray line broadening from filed aluminium and wolfram *Acta Metall.* **1** 22–31

[20] Iyyakkunnel S., Marot L., Eren B., Steiner R., Moser L., Mathys D., Düggelin M., Chapon P. and Meyer E. 2014 Morphological changes of tungsten surfaces by low-flux helium plasma treatment and helium incorporation via magnetron sputtering *ACS Appl. Mater. Interfaces* **6** 11609–16

[21] El-Atwani O., Gonderman S., Efe M., De Temmerman G., Morgan T., Bystrov K., Klenosky D., Qiu T. and Allain J.P. 2014 Ultrafine tungsten as a plasma-facing component in fusion devices: effect of high flux, high fluence low energy helium irradiation *Nucl. Fusion* **54** 083013

[22] Sharafat S., Takahashi A., Hu Q. and Ghoniem N. 2009 A description of bubble growth and gas release of helium implanted tungsten *J. Nucl. Mater.* **386–8** 900–3

[23] Donovan D., Buchenauer D., Whaley J., Wright G., Parish C. and Hu X. 2017 Characterization of he-induced bubble formation in tungsten due to exposure from an electron cyclotron resonance plasma source *Fusion Sci. Technol.* **72** 337–46

[24] Thompson M., Kluth P., Doerner R.P., Kirby N., Riley D. and Corr C.S. 2016 Measuring helium bubble diameter distributions in tungsten with grazing incidence small angle x-ray scattering (GISAXS) *Phys. Scr.* T **167** 014014

[25] Humphreys F.J. and Hatherly M. 2004 *Recrystallization and Related Annealing Phenomena* (Amsterdam: Elsevier)

[26] Bhatia M.L. and Cahn R.W. 1978 Recrystallization of porous copper *Proc. R. Soc.* A **362** 341–60

[27] Palacios T., Reiser J., Hoffmann J., Rieth M., Hoffmann A. and Pastor J.Y. 2015 Microstructural and mechanical characterization of annealed tungsten (W) and potassium-doped tungsten foils *Int. J. Refract. Met. Hard Mater.* **48** 145–9

[28] Ryabtsev S., Gasparyan Y., Efimov V., Harutyunyan Z., Aksenova A., Poskakalov A., Pisarev A., Kanashenko S. and Ivanov Y. 2019 Helium retention in tungsten irradiated with He + ion beam at elevated temperatures *Nucl. Instrum. Methods Phys. Res.* B accepted (https://doi.org/10.1016/j.nimb.2019.01.051)

[29] Hasson G. and Goux C. 1971 Interfacial energies of tilt boundaries in aluminium. Experimental and theoretical determination *Scr. Metall.* **5** 889–94

[30] Furu T., Ørsund R. and Nes E. 1995 Subgrain growth in heavily deformed aluminium—experimental investigation and modelling treatment *Acta Metall. Mater.* **43** 2209–32

[31] Vandermeer R. and Hansen N. 2008 Recovery kinetics of nanostructured aluminum: model and experiment *Acta Mater.* **56** 5719–27